Parameter-Free Test of Alloy Dendrite Growth Theory

Parameter-free test of alloy dendrite-growth theory

Craig B. Arnold* and Michael J. Aziz
Division of Engineering and Applied Sciences, Harvard University, Cambridge, Massachusetts 02138

Matthias Schwarz and Dieter M. Herlach
Institut für Raumsimulation, Deutsches Zentrum für Luft- und Raumfahrt, D-51170 Köln, Germany
(Received 18 May 1998)

In rapid alloy solidification the dendrite-growth velocity depends sensitively on the deviations from local interfacial equilibrium manifested by kinetic effects such as solute trapping. The dendrite tip velocity-undercooling function was measured in dilute Ni(Zr) over the range 1–25 m/s and 50–255 K using electromagnetic levitation techniques and compared to theoretical predictions of the model of Trivedi and colleagues for dendritic growth with deviations from local interfacial equilibrium. The input parameter to which the model predictions are most sensitive, the diffusive speed V_D characterizing solute trapping, was not used as a free parameter but was measured independently by pulsed laser melting techniques, as was another input parameter, the liquid diffusivity D_L. Best-fit values from the pulsed laser melting experiment are $V_D = 26$ m/s and $D_L = 2.7\times10^{-9}$ m^2/s. Inserting these values into the dendrite growth model results in excellent agreement with experiment with no adjustable parameters. [S0163-1829(99)02101-3]

I. INTRODUCTION

The physical state of solid matter strongly depends upon the conditions of formation. Normally, a system cooled below its melting temperature will crystallize under local equilibrium conditions. However, if a system is cooled beyond its melting temperature into the metastable regime of an undercooled melt, a great variety of solidification pathways are enabled. In particular, one can form metastable solid states such as supersaturated solid solutions, disordered superlattice structures, grain refined alloys, crystalline structures of metastable nature, or even metastable quasicrystalline and amorphous phases.[1] When an undercooled melt solidifies, the rejection of latent heat into the solid/liquid (s/l) interface causes an increase in the temperature near the interface. Since the temperature in the bulk of the melt is below the melting temperature, the result is a ''negative temperature gradient'' ahead of the interface. Similarly, there is a change in the concentration of alloys upon solidification that causes an additional concentration gradient ahead of the interface. Both of these effects tend to destabilize a planar s/l interface and can lead to dendritic growth.[2]

Deviations from local equilibrium at the s/l interface occur during rapid interface motion. Experiments have demonstrated a kinetic undercooling of the solidification front during rapid dendritic growth in undercooled melts of pure metals.[3] Alloy dendrite growth models introduce a kinetic undercooling term to account for this effect.[2,4,5]

In addition to a kinetic undercooling, deviations from chemical equilibrium at the s/l interface appear in rapid growth of solutal dendrites in alloys.[3,6] Kinetically suppressed partitioning at the interface is well described by the continuous growth model for solute trapping of Aziz and coworkers.[7–9] In the dilute concentration limit of alloys the velocity (V) dependence of the partition coefficient (k) is given by

$$k(V) = \frac{k_e + \dfrac{V}{V_D}}{1 + \dfrac{V}{V_D}}. \tag{1}$$

Here, k_e is the equilibrium partition coefficient and V_D is a parameter called the atomic diffusive speed, which is the growth rate at which k is in mid-transition between k_e and unity. This model has been experimentally verified for planar interfaces using pulsed laser melting techniques on a variety of different alloy systems.[9–12]

Models for solutal dendrite growth[2,4,5] assume that the continuous growth model holds for dendrites and that the only differences between the highly curved dendrite tip and the planar interface are the Gibbs-Thomson depression in the melting temperature and the solution for the diffusion field ahead of the moving interface. Their predictions for the relationship between V and undercooling (ΔT) depend very sensitively on the value of the input parameter V_D for both planar[13] and dendritic interfaces.[2] However, until now, in dendrite growth V_D has been used as a free parameter to fit the dendrite velocity-undercooling data.[14] The objective of the present work is to measure independently V_D and the dendrite velocity-undercooling function in the same alloy system, thereby eliminating this key free parameter and providing a rigorous test of theory. Additionally, we measure independently the bulk liquid diffusivity D_L thereby fixing the remaining free parameter used in the theory.

The most dramatic effect of the solute trapping transition is a sharp increase in the dendrite growth velocity at a critical velocity of $V_{cr} \approx 5$ m/s and a concentration-dependent critical undercooling, similar to that shown in Fig. 5(a). This effect has been studied for dilute Ni(B) and is interpreted as a transition from solutally controlled growth at small undercoolings to a pure thermally controlled dendrite at high undercoolings.[6]

In the present work an electromagnetic levitation technique is used to undercool bulk melts of $Ni_{99}Zr_1$ and to measure the growth velocity as a function of undercooling. A large undercooling range becomes accessible by this technique owing to the complete avoidance of container wall induced heterogeneous nucleation. In addition, pulsed laser melting experiments on thin films were used to measure independently V_D and D_L. The $Ni_{99}Zr_1$ alloy was chosen for the present studies because of several considerations. It is characterized by a small equilibrium partition coefficient k_e which is on the order of 10^{-2}. Therefore, a strong solute trapping effect is expected at growth velocities that are observable both in the undercooling experiments as well as in the laser resolidification experiments. Secondly, the precipitation of solvent-rich compounds, which would interfere with the measurement, is not strongly favored thermodynamically. An additional requirement for an accurate measurement of the partition coefficient k is the use of Rutherford backscattering spectrometry (RBS) depth profiling, which requires that the solute be significantly heavier than the solvent for good resolution. Finally, dilute Ni-base alloys such as $Ni_{99}Zr_1$ show an excellent undercooling behavior in experiments of containerless processing in an electromagnetic levitation coil due to its high melting temperature.[14]

II. EXPERIMENT

A. Levitation experiments

Electromagnetic levitation is used for containerless undercooling of bulk drops.[15] The experiments are conducted in an ultrahigh-vacuum (UHV) chamber which was evacuated to a pressure of 10^{-7} mbar and backfilled with a purified (purity better than 99.9999%) He-H_2 gas mixture (20 vol% H_2). Alloys of $Ni_{99}Zr_1$ were prepared from constituents of Ni and Zr; both of a purity better than 99.99%. These alloys were melted in situ by a radio frequency levitation coil into spheres of about 6 mm diameter with mass approximately 1 g. The location of the drop in the coil is shown in Fig. 1.

The conditions of containerless processing in a high purity gas atmosphere ensure high purity sample preparation. The temperature of the freely suspended drop is measured at its top by a two-color pyrometer with an absolute accuracy of ± 5 K and a measuring frequency of 100 Hz. The complete avoidance of container-wall induced heterogeneous nucleation and highly pure environmental conditions lead to reproducible maximum undercoolings of $\Delta T = 255$ K prior to nucleation.

Figure 1 also shows a temperature vs time profile as measured for the undercooled drop. After the onset of nucleation at a temperature $T_n = T_l - \Delta T$ the rapid release of the heat of crystallization during fast growth of dendrites results in a recalescence event. During this period, there exists a steep rise in the temperature up to a temperature between the liquidus T_l and solidus T_s temperatures. A very pronounced recalescence event is observed in the present levitation experiments because the undercooled melt acts as a heat sink for the released latent heat. Furthermore, heat transfer from the freely suspended drop to the environment is very limited since it has no contact with a liquid or solid medium. Heat is conducted only by thermal conductivity in the environmental

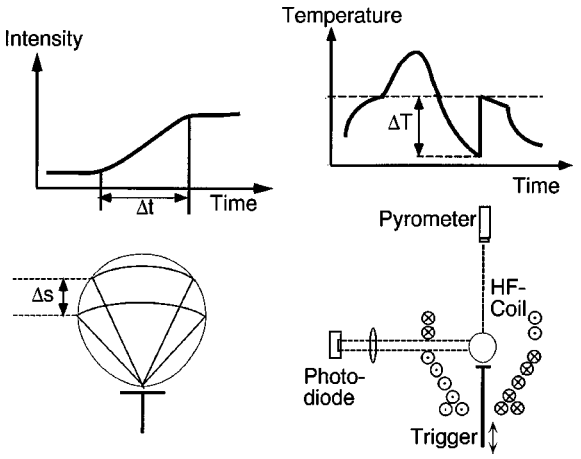

FIG. 1. Upper right: Temperature-time profile as measured contactless by pyrometry on an undercooled $Ni_{99}Zr_1$ sample freely suspended in an electromagnetic levitation coil. Lower right: Electromagnetic levitation coil showing the position of metal droplet with the pyrometer for temperature measurement and the photodiode for the velocity measurement. Lower left: The undercooled sample is externally nucleated by touching it at its lower bottom by an alumina needle. The photosensing device measures the time Δt needed by the array of dendrites to propagate through the observation window of the optical system. Upper left: Intensity versus time profile for the photodiode. The growth velocity is obtained from the ratio of the solidification path Δs taken by the solidification front and the time interval Δt.

gas and radiation. As a consequence, solidification takes place under quasiadiabatic conditions in levitation experiments.[16] Since the undercooling in the present experiments is large, most of the melt solidifies under nonequilibrium conditions during recalescence. Only a small volume fraction of remaining liquid crystallizes under near-equilibrium conditions at temperatures between T_l and T_s. The undercooling $\Delta T = T_l - T_n$ is directly determined from such a temperature-time profile.

Finally, the experimental setup for the velocity of the growing dendrite array is also shown in Fig. 1. At a preselected undercooling value, crystallization of the undercooled melt is stimulated at its lower end by touching it using an alumina stimuli needle. The solidification front starts at this well defined point at the surface of the sample and the array of dendrites grows radially into the melt. A rapid photosensing technique consisting of Si-photodiodes, an electronic amplifier, a transient recording system and an optical observation lens is used to measure the time Δt needed by the solidification front to propagate through the observation window. This technique is capable of measuring relative temperature changes with a frequency of 1 MHz. The growth velocity V is then easily determined by the ratio $\Delta s/\Delta t$ where Δs is the distance traveled by the s/l interface during time Δt.[17] At the largest undercoolings typical recalescence times of $\Delta t_{rec} \approx 100$ μsec are measured. Because of the rapid growth rates the thermal diffusion length ($2\times$thermal diffusivity/velocity) remains negligibly small during recalescence, permitting the velocity of the dendritic growth front to be inferred from the time-resolved photosensing measurements.

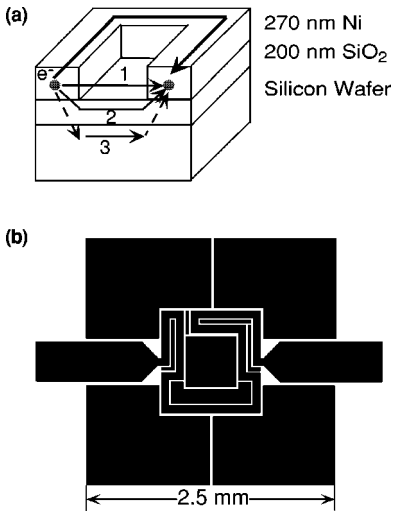

FIG. 2. Sample for pulsed laser melting and plane-front resolidification. (a) Cross section of sample with possible short-circuit pathways for electrical conduction shown. (1) Conduction through a plasma, (2) photoconduction through oxide layer, and (3) capacitive coupling to a molten layer of silicon below the exposed oxide layer. (b) Plan view of patterned sample showing large L/W ratio for resistance measurement and large central pad for reflection measurement.

B. Pulsed laser experiments

The diffusive speed and liquid diffusivity are independently measured by a pulsed-laser resolidification technique described elsewhere.[9–12] A thin film ($\sim$270 nm) of Ni (99.99% purity) was prepared by electron beam evaporation at 3 Å/sec under high vacuum conditions (base pressure $\sim 4\times10^{-7}$ mbar) on a thermally oxidized Si wafer (200 nm SiO_2) [see Fig. 2(a)]. Prior to deposition the substrate was sputter cleaned with Ar^+ ions (1.5 keV, 55 mA) for approximately 5 minutes. To help improve film adhesion to the substrate the ion beam was left running during the first minute of e-beam Ni deposition. The surface SiO_2 layer provides electrical isolation of the film from the silicon substrate, permitting time-resolved lateral electrical resistance measurements (''transient conductance measurements'') of the melt depth during melting and solidification. In addition, the reduced thermal conductivity of the oxide layer permits us to control the flow of heat out of the film during solidification by varying the oxide thickness. Therefore coarse grained control over the interface velocity is possible using different oxide thicknesses.

The Zr is introduced to the film by ion implantation of $^{90}Zr^+$. The energy and dose are chosen to yield a peak Zr concentration between 0.5 and 1 at. % centered at $\sim$30 nm beneath the free surface. After the films are prepared, the wafers are photolithographically patterned and sectioned for the transient conductance measurements (TCM). Figure 2(b) shows the pattern used for this experiment. The pattern is designed to provide a large length-to-width ratio ($L/W \approx 65.5$) to make contact resistances negligible and to provide a large uniform area for the reflectance measurement.

The geometry of the laser resolidification experiment is shown in Fig. 3. The laser melting was performed with a single 28 ns excimer laser pulse (KrF:$\lambda = 248$ nm) at fluences between 0.4–0.7 J/cm^2. Such fluences yield solidification velocities between 2–3 m/s. A second laser (Ar^+ laser $\lambda = 488$ nm) was used to probe the transient reflectance while a dc voltage source supplied the sample bias for the transient resistance measurement. Both the resistance and reflectance measurements were acquired on a multichannel digitizing oscilloscope (Tektronics model TDS 620) at a rate of 2GSamples/sec. This sampling rate is sufficiently fast to resolve events occurring on the nanosecond time scale.

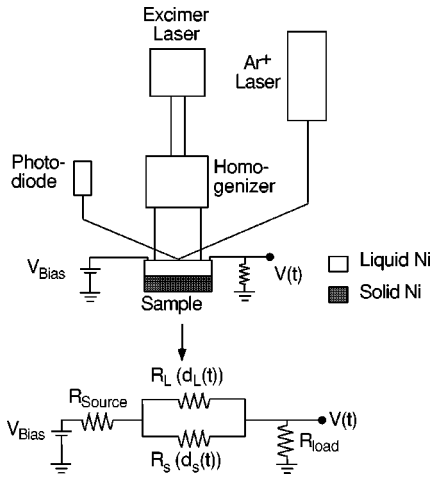

FIG. 3. Laser melting setup. When partially molten, the sample is treated as two resistors in parallel. $V_{bias}=10$ V, $R_{source}=R_{load}=50\Omega$.

The initial and final concentration profiles of Zr were obtained using RBS grazing-angle technique.[12] For this experiment, it was necessary to use relatively high energy 3 MeV He^{++} to fully resolve the Ni and Zr peaks resulting in a depth resolution of 11.5 nm. In addition, the absolute calibration of the spectra is critical for proper analysis of the segregation behavior. All samples were self-calibrated using the ^{58}Ni, Si, and O edges. The latter two elements were usable because the photolithographic patterning exposed some bare oxide to the RBS beam.

Finally, the analysis of the liquid diffusivity and diffusive speed was performed by comparing the measured final concentration profile to one predicted by computer simulation. The simulation utilized a Crank-Nicholson algorithm to solve the one-dimensional diffusion equation for the molten portion of the sample while taking into account the segregation at the interface. The values of the liquid diffusivity and the diffusive speed are then determined by a best fit between the experimental and simulated curves. We have utilized a normalized χ^2 test to determine the best fit between the two curves according to the equation

$$\chi^2=\frac{1}{N-1}\sum_{i=1}^{N}\frac{[\exp(x_i)-\mathrm{sim}(x_i)]^2}{[\mathrm{uncert}(x_i)]^2}.$$

Here, N is the total number of data points, x_i is the depth for a particular data point i, $\exp(x)$ is the experimentally measured concentration, $\mathrm{sim}(x)$ is the simulated concentration, and $\mathrm{uncert}(x)$ is the uncertainty in the measured concentration at that depth. In this case, the uncertainty derives from the statistical uncertainty in the RBS measurement. Thus the uncertainty should be the square root of the number of counts in a given channel. However, the uncertainty

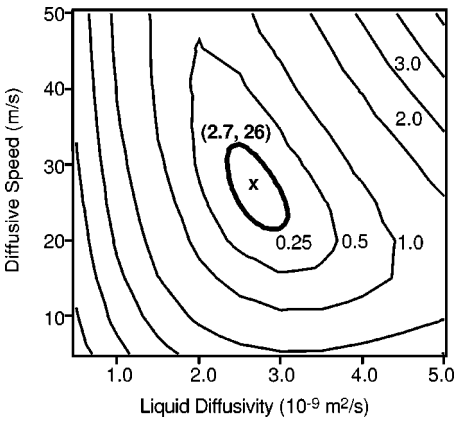

FIG. 4. χ^2 plot showing best-fit values for $V_D=26$ m/s and $D_L=2.7\times10^{-9}$ m^2/s and their uncertainties. The dark line surrounds the region of best fit. Thinner lines denote contours of less satisfactory agreement.

cannot be less than the background level for the RBS spectrum. For this particular experiment, the background level was 0.012 at. %. As with all χ^2 tests, the lower value for χ^2 corresponds to the best fit between the two curves. Figure 4 shows a contour plot of χ^2 as a function of the diffusive speed and the liquid diffusivity. The minimum value occurs for the values of $V_D=26$ m/s and $D_L=2.7\times10^{-9}$ m^2/s with the region of good fit denoted with a solid line.

III. EXPERIMENTAL RESULTS AND DISCUSSION

A. Analysis of dendrite growth velocities

Figure 5(a) shows the experimental results for the measurements of the dendrite growth velocity as a function of undercooling ΔT on dilute $Ni_{99}Zr_1$ alloy. The results of the measurements are represented by the closed dots. At small undercoolings the growth velocity is rather sluggish. However, when the undercooling ΔT approaches a critical value of $\Delta T_{cr}\approx160$ K a steep rise of the growth velocity with increasing undercooling is observed. Qualitatively similar behavior in the velocity versus undercooling relation was previously observed in dilute Ni-B alloys.[6]

For an analysis of the experimental data we apply current theories of alloy dendrite growth in undercooled melts.[2,4,5] Correspondingly, the total undercooling ΔT is expressed as the sum of four different terms,

$$\Delta T=\Delta T_t+\Delta T_c+\Delta T_r+\Delta T_k, \tag{2}$$

where the individual contributions are: the thermal undercooling ΔT_t; the kinetic constitutional undercooling ΔT_c, which includes both the effects of composition gradients in the melt ahead of the interface and composition changes in the solid due to solute trapping; the curvature undercooling ΔT_r; and the kinetic interface friction undercooling ΔT_k. These are expressed as

$$\Delta T_t=\frac{\Delta H_f}{C_p^l}\mathrm{Iv}(P_t), \tag{3}$$

$$\Delta T_c=m_e c_0\left[1-\frac{m_L(V)/m_e}{1-(1-k(V))\mathrm{Iv}(P_c)}\right], \tag{4}$$

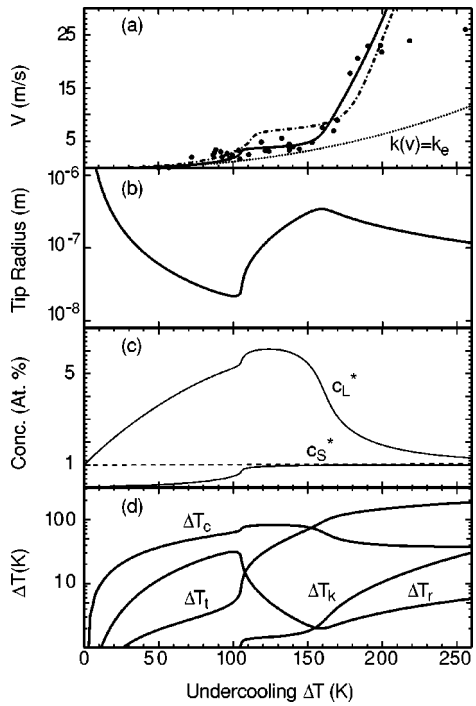

FIG. 5. Dependence on total bath undercooling of various quantities. (a) The dendrite growth velocity, as measured on $Ni_{99}Zr_1$ alloy (dots). The solid line gives the prediction of dendrite growth theory using the values $V_D=26$ m/s and $D_L=2.7\times10^{-9}$ m^2/s from Fig. 4. For comparison, the dotted line represents the calculated growth velocity if no solute trapping is taken into account. The dot-dashed lines give the results of calculations for values $V_D=50$ m/s and $D_L=5.0\times10^{-9}$ m^2/s, values that are within typical ranges for metallic systems but are not near the minimum χ^2 in Fig. 4. These latter two curves demonstrate the importance of an accurate knowledge of V_D and D_L for modeling alloy dendrite growth. All curves in (b)–(d) use $V_D=26$ m/s and $D_L=2.7\times10^{-9}$ m^2/s. (b) The dendrite tip radius calculated on the basis of the marginal stability analysis of growing dendrites. (c) The concentrations c_L^* and c_S^* of the liquid and solid at the interface computed within dendrite growth theory. (d) Semilog plot of the individual undercooling contributions: thermal undercooling ΔT_t, constitutional undercooling ΔT_c, curvature undercooling ΔT_r, and kinetic interface undercooling ΔT_k. These curves are calculated using Eqs. (3)–(6).

$$\Delta T_r=2\frac{\Gamma}{r}, \tag{5}$$

$$\Delta T_k=\frac{V}{\mu}. \tag{6}$$

Here, $\mathrm{Iv}(x)=x\exp(x)\mathrm{E}_1(x)$ denotes the Ivantsov function with E_1 the first exponential integral function; $P_t=(Vr)/2D_T$ is the thermal Péclet number with r the radius at the tip of a dendrite and D_T the thermal diffusivity; m_e is the slope of the equilibrium liquidus; $m_L(V)$ is the slope of the kinetic liquidus; c_0 is the nominal concentration of the alloy; $P_c=(Vr)/2D_L$ denotes the solutal Péclet number with D_L the liquid diffusion coefficient; $\Gamma=\sigma/\Delta S_f$ is the Gibbs-Thomson coefficient with σ the solid-liquid interface tension, $\Delta S_f=\Delta H_f/T_L$ the entropy of fusion, ΔH_f the enthalpy of fusion and T_L the liquidus temperature; and $\mu=(\Delta H_f V_0)/(R_g T_L^2)$ denotes the interfacial kinetic growth

coefficient for pure solute with R_g the universal gas constant. If we assume the validity of the collision limited growth model,[18] the factor V_0 in the expression for μ is set equal to the speed of sound V_s as an ultimate limit of the growth velocity, $V_0 = V_s$. This means that the atomic vibration frequency, which is of the order of 10^{13} Hz, gives the relevant time scale for the attachment kinetics of the atoms at the s/l interface and not the atomic diffusion frequency which is much slower. The collision limited growth model has been shown experimentally to be a good approximation for modeling the interface undercooling of Ni-based alloys forming fcc structure.[3,6,19]

The interfacial tension σ is estimated using the negentropic model developed by Spaepen[20,21]

$$\sigma = \alpha \frac{\Delta S_f}{N_L^{1/3} V_M^{2/3}} T, \tag{7}$$

with N_L Avogadro's number, V_m the molar volume and α, a factor that depends on the structure of the solid phase. Since a $Ni_{99}Zr_1$ solid solution crystallizes into fcc structure, $\alpha = 0.86$.

The quantity $m_L(V)$ in Eq. (4) merits special attention. It represents the dependence of the slope of the kinetic liquidus curve[8] on the velocity. As the velocity increases, the liquidus and solidus lines approach each other and coincide in the case $k(V) = 1$.[8] For dilute solutions $m_L(V)$ is determined by[5]

$$m_L(V) = m_e \left[\frac{1 - k(V) + k(V) \ln(k(V)/k_e)}{1 - k_e} \right]. \tag{8}$$

It is worth noting that Eq. (8) is the same expression as developed by Aziz and Boettinger in their model of a transition from a low mobility to a high mobility interface in the absence of solute drag.[13]

Equations (2)–(6) describe the undercooling in terms of the product of the growth velocity times the dendrite tip radius. For a unique calculation of V as a function of undercooling, ΔT, we utilize the criterion of marginal stability[22,23] which gives an independent expression of the dendrite tip radius:

$$r = \frac{\Gamma}{\sigma *} \left[2\pi \bar{\kappa} \frac{\Delta H_f}{C_p^l} P_t \xi_t - \frac{2 m_e c_o (1 - k(V))}{1 - (1 - k(V)) \mathrm{Iv}(P_c)} P_c \xi_c \right]^{-1}, \tag{9}$$

where C_p^l is the specific heat for the liquid; $\bar{\kappa}$ is defined as

$$\bar{\kappa} = \frac{\kappa_L}{\kappa_L + \kappa_S} \tag{10}$$

with κ_L and κ_L the thermal conductivity of the liquid and solid, respectively;

$$\xi_t = 1 - [1 - (2\pi / P_t)^2]^{-1/2}, \tag{11}$$

$$\xi_c = 1 - \frac{2k(V)}{2k(V) - 1 + (1 + (2\pi / P_c)^2)^{1/2}}, \tag{12}$$

and the value of the ''stability parameter'' taken from the marginal stability criterion,

$$\sigma^* = \frac{1}{4\pi^2}. \tag{13}$$

Equation (9) emphasizes the importance of $k(V)$ for the stability analysis of a rapidly growing dendrite. This means that the parameters V_D and D_L not only affect the constitutional undercooling but also the marginal stability of a growing dendrite in an essential way.

The validity of Eq. (13) has been supported by previous measurements of the growth velocity as a function of undercooling for pure Ni and Ni-Cu alloy.[3] Recent advances in so-called ''solvability theory'' show that the marginal stability criterion is not rigorous and lead to the modification of Eq. (13) by an anisotropy parameter. This factor is assumed to be unity for cubic systems, thereby permitting the continued use of Eq. (13). However, there is experimental and theoretical evidence that in alloys, σ^* may depend on the undercooling as well as on composition.[24,25] Because Eq. (13) has been shown to hold for both pure Ni and Ni-30 at. % Cu in Ref. 3, we assume that the addition of a small amount of Zr to pure Ni does not have a significant effect on σ^*. Our measurements do not have the sensitivity to discern a temperature dependence in σ^*: if the dependence of σ^* on relative undercooling is assumed comparable to that in xenon,[26] then the predicted change in the $V(\Delta T)$ relationship is roughly equal to the uncertainty of the present measurements. In effect, because we are assuming σ^* to be constant and given by Eq. (13), our experiment can be considered a test of marginal stability theory. Once they become available, predictions of solvability theory for alloys may also be compared with the data. We expect any differences to be minor in the vicinity of ΔT_{cr}, which is the most important region for the purpose of this study.

To obtain numerical values for the theoretical prediction for $V(\Delta T)$, the values of V_D and D_L are taken from independent laser resolidification experiments on thin films. The best fit values of $V_D = 26$ m/s and $D_L = 2.7 \times 10^{-9}$ m^2/s were used. The numerical values of the various parameters used in the calculations are listed in Table I. There are two other parameters which are not measured independently in this experiment. These were obtained from the literature but are not known very well. (1) V_0, the speed of collision-limited growth at infinite driving force, which we assume to be equal to the speed of sound according to Turnbull's collision-limited growth model, and take it to be 4000 m/s.[27] The predictions are highly insensitive to the precise value of V_0 provided that V_0 remains much higher than the maximum measured dendrite speed. (2) The equilibrium partition coefficient is known to be very small, of order 10^{-2}, but it has not been measured accurately. We measured the liquidus curve over the range 0–3 at. % Zr using differential scanning calorimetry; we then obtained a value of k_e by fitting a parabola to three points along the reported solidus curve,[28] combining the result with our measured liquidus curve, and extrapolating to the dilute limit. The resulting value of $k_e = 3 \times 10^{-2}$ was used in our solidification simulations. On the scale of the scatter in the experimental data, the predictions of the model at low undercoolings are not highly sensitive to the value of k_e input.

The solid line in Fig. 5(a), obtained with the numerical values of the parameters as described above, results in an

TABLE I. Material parameters used for the calculation of the dendrite growth velocity V, the tip radius r, and the concentration in liquid at the interface c_L^* as a function of undercooling ΔT for $Ni_{99}Zr_1$ alloy. m_e was determined by differential scanning calorimetry (DSC) studies on three different samples $Ni_{99.5}Zr_{0.5}$, $Ni_{99}Zr_1$, and $Ni_{98.5}Zr_{1.5}$. D_T was calculated using measured values of the electrical resistivity in the undercooled melt regime of Ni-Zr alloys (Ref. 35) and assuming the validity of the Wiedemann-Franz law. $\overline{\kappa}$ was calculated using Eq. (10) with values from Refs. 36 and 37.

Parameter	Symbol	Dimension	Value
Heat of fusion	ΔH_f	(J/mol)	17 150[a]
Specific heat of liquid	C_p^l	(J/mol K)	41[a]
Liquidus temperature	T_l	(K)	1714[a]
Slope of equilibrium liquidus	m_e	(K/at. %)	-14[a]
Thermal diffusivity	D_T	(m^2/s)	9×10^{-6}
Effective thermal conductivity	$\overline{\kappa}$	none	0.27
Equilibrium partition coefficient	k_e	none	0.03[b]
Limiting speed of collision-limited growth	V_0	(m/s)	4000[c]
Diffusion coefficient	D_L	(m^2/s)	2.7×10^{-9}
Atomic diffusive speed	V_D	(m/s)	26

[a]Values determined by high-temperature DSC measurements (Ref. 38).
[b]Reference 28.
[c]Reference 27.

excellent agreement with the measured data for $V(\Delta T)$. In order to test the reliability of this analysis an additional $V(\Delta T)$ curve was calculated for values of V_D and D_L which correspond to worse fits of the laser resolidification experiment but still fall within the range of observed pairs of numerical values of V_D and D_L for metallic systems.[9–12] It is clear that such numbers lead to strong deviations between the calculated and experimentally measured dendrite growth velocities as a function of undercooling. This result emphasizes the importance of reliable values for V_D and D_L for a quantitative description of the dendrite growth velocity versus undercooling relation.

The dotted line in Fig. 5(a) gives the prediction of dendrite growth theory if k is assumed to be independent of V. Deviations between the data and the prediction become appreciable for $\Delta T>100$ K. At undercoolings $\Delta T>160$ K, these deviations become very pronounced. This further indicates the need to accurately take solute trapping into account.

This behavior can be understood by considering the dependence of the radius of curvature at the dendrite tip on the undercooling. Figure 5(b) shows r as a function of undercooling ΔT. At small undercoolings ($\Delta T<100$ K), r decreases very rapidly with increasing undercooling. In this regime the concentration gradient ahead of the s/l interface controls the tip radius r. The higher the velocity the deeper the concentration gradient and, consequently, the smaller the tip radius. At very small undercoolings, solute trapping begins moderately which leads to slight deviations from chemical equilibrium at the interface. This trapping causes an equivalent reduction of the concentration gradient with a corresponding change in r, which is now passing through a minimum. If undercooling is further increased solute trapping becomes even more important and the tip radius increases since the concentration gradient flattens out until the absolute stability of a solutally controlled dendrite is reached. At this undercooling the tip radius goes through a maximum. Beyond this maximum, the size of the tip radius is exclusively governed by the thermal gradient since the concentration gradient disappeared due to complete segregation free solidification. The behavior of the tip radius as a function of undercooling also reflects the fact that the chemical diffusion coefficient and the thermal diffusivity differ by about three orders of magnitude (cf. Table I). Therefore, the concentration boundary layer is much thinner than the thermal boundary layer ahead of an advancing s/l interface.

We investigate the change in the concentration of the liquid as a further analysis of solute trapping and its consequence on the growth of dendrites in undercooled melts. The concentration in the liquid just in front of the interface c_L^* is quantitatively determined within alloy dendrite growth theory by[3]

$$c_L^* = \frac{c_0}{1-(1-k(V))\mathrm{Iv}(P_c)}. \tag{14}$$

The concentration in the solid at the interface c_S^* is then found by applying the definition of the partition coefficient, $c_S^* = k(V)C_L^*$. The results of computations using Eq. (14) are exhibited in Fig. 5(c) as a function of undercooling. At small undercoolings the Zr concentration in the liquid rises due to the rejection of the solute atoms (very limited equilibrium solubility in the solid phase) and the concentration profiles follow the equilibrium values. This means there is strong partitioning in front of the advancing interface for undercoolings $\Delta T<70$ K. If the undercooling is increased into the regime $\Delta T>70$ K, deviations occur that progressively increase with undercooling. At large undercoolings $\Delta T>\Delta T_{\mathrm{cr}}=160$ K, c_L^* and c_S^* approach the nominal concentration c_0 of the alloy. This means that at such large undercoolings we have reached a regime of complete solute trapping.

We use the above information to understand the velocity-undercooling relation. At small undercoolings the interface

movement is sluggish (low mobility of the interface) and controlled by the redistribution of solute in front of the interface. When solute trapping becomes important, the concentration gradient becomes weaker until it disappears for undercoolings above $\Delta T_{cr}=160$ K. In this large undercooling regime, the constitutional undercooling loses its influence and the growth velocity is only controlled by the thermal gradient in front of the s/l interface. This enables the interface to move much faster (high mobility of the interface) since the thermal diffusivity is three orders of magnitude greater than the chemical diffusivity. Thus, the growth velocity steeply rises in the transition regime around ΔT_{cr}.

The transition from solutally controlled to thermally controlled dendrite growth is also reflected in Fig. 5(d) where the individual undercooling contributions are plotted as a function of the undercooling. These plots are calculated using Eqs. (3)–(6). One can see that the curvature undercooling, ΔT_r, is of minor importance for undercoolings $\Delta T > 160$ K. The thermal undercooling, ΔT_t, and the kinetic undercooling, ΔT_k, continuously increase with the total undercooling ΔT. Here the rise of the kinetic undercooling is less pronounced than that of the thermal undercooling. The constitutional undercooling ΔT_c behaves quite different. At small undercoolings $\Delta T<120$ K, ΔT_c strongly rises with ΔT. However, when the total undercooling exceeds $\Delta T = 120$ K, ΔT_c decreases and eventually approaches a constant value, determined by the difference in slope between the equilibrium liquidus and the kinetic liquidus [$\Delta T_c \rightarrow (m_L - m_L(V))c_0$]. Here, crystallization is almost completely partitionless, i.e., $k \gg 1$.

B. Measurements of the diffusive speed and the liquid diffusion coefficient

Although Fig. 4 shows the final results for our fit of V_D and D_L to the experimental data, we need to look carefully at the analysis before we can fully understand these results. There are three important pieces of information we need to obtain from the experiment: (1) a melt history which gives the position of the interface as a function of time, (2) a concentration profile as a function of depth for the sample before laser irradiation, and (3) a concentration profile as a function of depth for the sample after laser irradiation. We can use the first two pieces of information to simulate a final concentration profile using the technique described in Sec. II B and compare this profile to the experimentally measured profile.

We use the sharp change in the reflectance and resistance when a material undergoes a transition from a solid to a liquid state in order to measure the melt history.[12,29,30] The measurement of the reflectance provides the exact time when the film first begins to melt. Furthermore, the resolidification of the surface is characterized by another sharp jump in reflectivity followed by a gradual rise as the solid film cools. The resistance measurement provides information about the depth of the interface as a function of time. Figure 6 shows the measured reflectance curve that exhibits both of these transitions as well as the measured resistance curve. When the film begins to melt, the resistance rises since the resistivity of liquid metal is higher than that of solid metal. For Ni, the resistivity increases approximately 30% upon melting. Eventually, the interface reaches a maximum depth and the

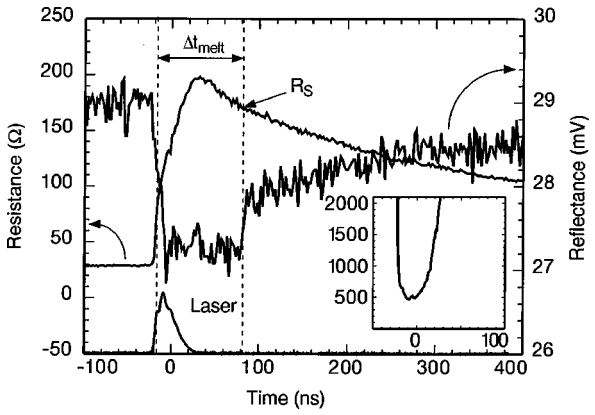

FIG. 6. Transient resistance and reflectance of thin film sample during pulsed laser melting. In addition, the laser intensity (arb. units) as a function of time is shown. R_S denotes the resistance of a fully solid film at its melting temperature, while Δt_{melt} shows the melt duration of ~100 ns. The inset depicts the parasitic conductance produced from a sample with a broken conduction circuit. The conductance persists during the presence of the laser pulse but dies shortly thereafter.

film begins to resolidify. This is characterized by a decrease in the resistance as the film returns to the solid state.

If the interface is planar and parallel to the free surface then we can model the sample resistance as two resistors in parallel: a liquid metal resistor and a solid metal resistor, each with a resistance R given by

$$R(t)=\frac{\rho}{d(t)}\frac{L}{W}, \tag{15}$$

where $d(t)$ is the time-dependent thickness of the (solid or liquid) layer, ρ is the resistivity of the phase, and L/W is the length-to-width ratio of the patterned sample. We then apply Kirchoff's laws to the circuit as shown in Fig. 3 to convert the resistance versus time data into the melt depth versus time data. We obtain the equation:

$$D_L(t)=\frac{R_L D\left(\dfrac{R_S}{R_{\text{sample}}(t)}-1\right)}{R_S-R_L}, \tag{16}$$

where R_S is the resistance of a fully solid film at the melting temperature, R_L is the resistance of a fully liquid film at the melting temperature, D is the total thickness of the metal film, and $R_{\text{sample}}(t)$ is the resistance of the sample as measured. In the above equation, both R_S and R_L need to be determined by the experiment. R_S is easily found if we use the information contained in the reflectance profile. The reflectance profile tells us the time when the film resolidifies and therefore, the resistance at this time is R_S. In an ideal experiment, the resistance at the beginning of the melt should be the same as the resistance at resolidification since in both cases, the film is a solid at its melting temperature. However, as we can see in Fig. 6, this is not the case for our system. We observed a suppression in the sample resistance at the beginning of the melt.

The reason for the suppression in the resistance is related to an alternate conduction path that is excited by the laser pulse. The inset in Fig. 6 shows the resistance curve for a

sample for which the normal conduction path in Fig. 2(b) has been broken. In this case, when we irradiate the sample with the same fluence as in Fig. 6, we still observe conductance despite the broken film. Once the laser intensity decreases, the conductance decreases until the circuit returns to its open state. Three possible conduction pathways are shown in the cross section of the sample in Fig. 2(a). These include (1) formation of a plasma above the surface, (2) excitation of electron-hole pairs in SiO_2, and (3) melting of silicon below the oxide. If a plasma were to form, we would expect to see some sharp effect in the reflectance trace owing to the change in reflectivity induced by the plasma.[31] However, Fig. 6 does not show any clear sign of plasma formation. Additionally, the band gap in SiO_2 is approximately twice the photon energy (band gap 8–10 eV compared to a photon energy of 5 eV for KrF). Therefore photoconduction would require a multiple photon effect which should make this a relatively minor effect.

We believe pathway (3) to be the most probable source for the parasitic conductance. If there is enough transmission of energy through the oxide layer, either by having a thin oxide layer or a high initial energy, it is possible to melt a thin layer of the underlying silicon.[32] Upon melting, the Si becomes conductive with a resistivity approximately that of the Ni film ($\rho = 80$ mW cm). When the resistance of the metal film changes rapidly upon irradiation, the local voltage changes can be capacitatively coupled into the underlying conductive Si layer. This alternate conductive path would tend to lower the apparent resistance of the circuit, thereby producing the suppressed peak we see in Fig. 6. This effect was not reported in previous laser melting experiments on metals;[12,33] however, these earlier experiments employed lower melting-point metals (and correspondingly lower laser intensities for melting) or different laser wavelengths (XeCl, $\lambda = 308$ nm or ruby, $\lambda = 694$ nm).

In order to use the resistance curve to determine the melt history, we assume that the resistance on the resolidification side of the curve is artifact-free because by the time solidification starts the laser pulse has long ended. To find the resistance of the fully solid film at the melting point, we determine the moment at which resolidification is complete from the reflectance curve and look up the solid resistance at that moment. With this method we must make assumptions for the initial melting portion of the melt history. However, our results are not sensitive to these assumptions, as the melt-in speed must be very high and all the important solute effects occur during the solidification interval when the interface has encountered the solute profile, which occurs within 100 nm of the surface.

The resistance of the liquid film at the melting point is harder to obtain from the experiment. Noise and parasitic conductance prevent us from using either the reflectance or the conductance technique to determine the first moment when the film has fully melted. Once the film is fully molten and the parasitic conductance paths go away, in principle it might be possible to determine the resistance of the liquid at the melting point if one could identify the moment that solidification commences. However, the moment at which the liquid film crosses the melting point may be different because liquid undercooling may occur before solidification of a fully molten film, as shown by Atwater *et al.* who undercooled liquid Ni by more than 500 K with pulsed laser melting.[33] Therefore we cannot measure the liquid resistivity at the melting point directly in this experiment, and in order to determine the melt history we must make assumptions about its value. We assume that the ratio of liquid resistivity to solid resistivity at the melting point in our films has the same value, $\rho_L/\rho_S = 1.299$, as for bulk pure Ni. This assumption (i.e., scattering from interfaces and extended defects is negligible compared with phonon scattering) has been shown to work well for pulsed laser melting of thin films of pure Ni.[33] Here the additional assumption is that solution scattering from the small amount of solute that we have, which is confined to a restricted portion of the entire film, is negligible compared to phonon scattering at the melting point. With this assumption we can rewrite Eq. 16 in terms of R_S and ρ_L/ρ_S, resulting in an equation with no more unknowns:

$$D_L(t) = \frac{\frac{\rho_L}{\rho_S} D\left(\frac{R_S}{R_{\text{sample}}(t)} - 1\right)}{1 - \frac{\rho_L}{\rho_S}}. \tag{17}$$

In using this equation we are making the additional assumption that the resistivities of the fully solid and fully liquid thin film at the melting point, and not merely their ratio, are the same as those for bulk material. This is tantamount to using the length-to-width ratio in our photolithographically patterned samples as an adjustable parameter. Because the patterned lines are narrow, small variations in line width (caused, for example, by small variations in etch strength from run to run) can cause small variations in L/W. The value that we obtain from fitting to Eq. (15), $L/W = 69.7$, is close to the ''nominal'' value of 65.5 and is within the uncertainty of measurements made on micrographs of actual samples.

Figure 7 shows the actual melt profile as calculated by the above analysis. For the earlier time stages, we have used a simulated profile that was calculated using a one-dimensional heat-flow code that has been well calibrated for

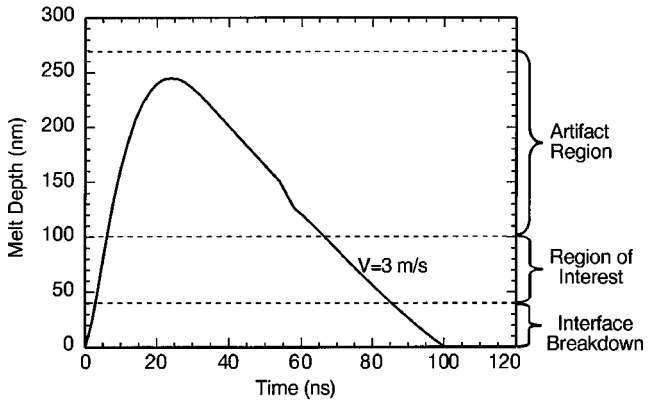

FIG. 7. Melt history deduced from conductance shown in Fig. 6. Region of interest (40–100 nm), from which V_D and D_L are deduced, is free of conductance artifact and of nonplanar growth. Artifact region deeper than 100 nm is solute-free and therefore not of interest; surface region shallower than 40 nm is nonplanar growth and therefore not tractable.

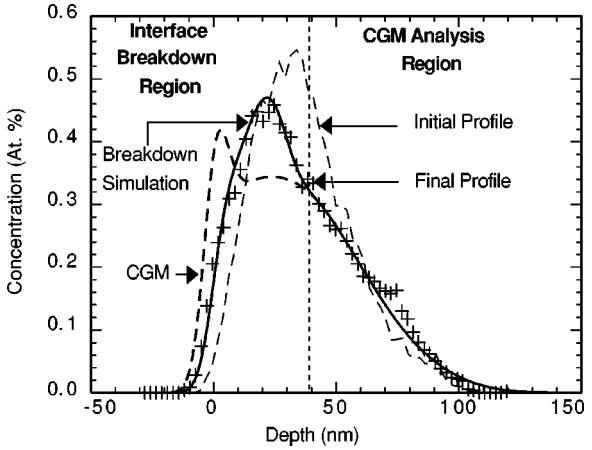

FIG. 8. Zr concentration vs depth profiles before (light dashes) and after (+) resolidification, used to determine V_D and D_L. Heavy-dashed curve is a simulation with CGM [Eq. (1)] over the entire depth using the values of $V_D=26$ m/s and $D_L=2.7\times10^{-9}$ m^2/s. The solid curve assumes CGM for depths >40 nm and an effective $k(t)$ given by Eq. (16) for depths <40 nm. The same values for V_D and D_L are used with $t=3.5$ ns.

pure Ni films on oxidized Si wafers.[33] This region, in which we cannot determine the melt history experimentally for the reasons describe above, is denoted the ''artifact region.'' During the initial melting segment of the experiment, the interface moves very quickly through the region of interest with a velocity of $V\gg17$ m/s. A significant amount of liquid diffusion occurs before the interface returns during resolidification. The interface velocity during solidification is approximately 3 m/s, which is sufficiently fast for measurable solute trapping effects to occur.

The final step in this experiment is to perform one-dimensional diffusion simulations[12] to determine the diffusive speed and the liquid diffusivity. Figure 8 shows the initial concentration profile and the post irradiation concentration profile along with two simulation curves representing our best fit values for V_D and D_L. The dark-dashed line shows a simulation using the CGM over the entire region of resolidification. It is evident from the figure that although the simulation fits the depth profile for the deep region fairly well, it does not reproduce the data in the near surface region ($z<40$ nm). It is likely that this discrepancy in the data is because our assumption of a planar interface throughout solidification does not apply. With an interface that is planar and parallel to the free surface, Zr is transported toward the surface by segregation at the interface during solidification. If the interface becomes unstable and breaks down into, for example, a cellular structure, some Zr transport will be parallel to the surface and less Zr will ultimately reach the surface. Our depth profile measurements detect a lateral average over ~2 mm and are unable to resolve lateral variations on the submicron size scale of cellular breakdown.

Interface stability under laser melting has been studied quantitatively by Hoglund *et al.* for the Si-Sn system.[34] In their samples an initially planar interface became unstable at approximately 50 nm below the surface, resulting in the laterally-averaged measured concentration profile diverging at this point from the profile simulated assuming a planar interface. In our case, the divergence between simulated and measured profiles starting at approximately 40 nm below the surface can be explained by interfacial breakdown commencing at this point. We believe this to be the cause of the divergence, although we were unable to verify this by observing a cellular microstructure in TEM. Such observations are quite difficult because the lateral scale of the breakdown is predicted to be only in the nanometer range (for example, Hoglund *et al.* observed 60 nm cells in Si-Sn), and ion milling results in sputter-induced surface rippling with features in the same size range.

In order to lend more plausibility to our interpretation in the absence of a direct observation of a cellular microstructure, we performed a simple simulation of the apparent one-dimensional concentration-depth profile caused by segregation during interfacial breakdown. The simulation is merely a simplification for the much more complicated three-dimensional problem associated with diffusion and partitioning at an unstable interface, which is beyond the scope of this work to fully address. We assume that the interface remains planar for $z>40$ nm and therefore k is given by the CGM [Eq. (1)]. In the near surface ''interface breakdown'' region ($z>40$ nm), we simulate growth using a planar interface with an effective k that is higher than the value given by the CGM. In the breakdown region, where the amplitude of a sinusoidal interface shape perturbation is expected to grow exponentially in time, we assume that the effective k increases exponentially with time as the lesser of unity and

$$k_{\mathrm{eff}}(t)=k(t_0)\exp\left(\frac{t-t_0}{\tau}\right), \tag{18}$$

where t_0 is the time at which the solidification front passes $z=40$ nm and τ is a free parameter determined by fitting the data. The solid line in Fig. 8 shows the result of this simulation. The use of this approximation in the near surface region and the CGM in the deeper region provides a qualitatively good fit over the entire depth range. For the purposes of obtaining V_D and D_L, we disregard the near-surface region of the curve and limit our quantitative analysis to the region over which the interface is believed to be planar. The cost of limiting our region of interest is an increased uncertainty in the value of V_D determined by the technique. The size of the surface peak in a post irradiated concentration profile is strongly dependent on V_D. Therefore by ignoring this region of the plot, we end up with larger, but still tolerable, error bars on V_D.

Ignoring the surface region in the simulation curves in Fig. 8, we may still distinguish between a good fit and a poor fit in the deeper region. In order to quantify this fit we have applied a χ^2 test between the experimental curve and the simulated curve in the region 40 nm$\leqslant z<100$ nm. Additionally, because there is a small peak in the experimental curve in this region from an Au impurity localized at the Ni/SiO_2 interface, for the comparison shown in Fig. 4 the depth range 67–83 nm was excluded from the chi-square analysis.

IV. SUMMARY

(1) Dendrite $V(\Delta T)$ measurements in Ni(Zr) were made with electromagnetic levitation and rapid photosensing tech-

niques. The results show qualitatively the transition from a thermal to a solutal dendrite as solute trapping effects set in.

(2) The quantitative predictions of alloy dendrite growth theories for $V(\Delta T)$ at high V, where nonequilibrium interface kinetics are important, depend sensitively on the numerical value of V_D characterizing solute trapping.

(3) Pulsed laser melting of thin films of Ni(Zr) was used to determine V_D and D_L independently. Interface breakdown in the near-surface region prevents us from deriving useful information about V_D and D_L from that region but does not prevent us from determining V_D and D_L from the nonbreakdown region. Best-fit values are $V_D = 26$ m/s and $D_L = 2.7 \times 10^{-9}$ m^2/s.

(4) The uncertainties in V_D and D_L are coupled and are shown graphically in Fig. 4.

(5) Inserting the best-fit values of V_D and D_L into the model of Trivedi and colleagues for dendritic growth with deviations from local interfacial equilibrium results in excellent agreement with the $V(\Delta T)$ measurements [Fig. 5(a)]. Although some of the parameters are not known very accurately, none of them are treated as adjustable parameters in the comparison with experiment.

(6) Laterally-averaged segregation in the region where interface breakdown occurred can be modeled roughly as a planar interface with a partition coefficient increasing exponentially with time until it reaches unity.

ACKNOWLEDGMENTS

The authors thank Dr. K. Eckler for stimulating discussions. Work at Harvard University was supported initially by NSF-DMR-92-08931 and subsequently by NASA-NAG8-1256. Financial support by the Deutsche Forschungsgemeinschaft within Contract No. He 1601/4-2 is gratefully acknowledged. In addition, one of us (C.B.A.) acknowledges the support of ONR. D.M.H. expresses his sincere gratitude to Professor M. J. Aziz and Professor F. Spaepen for their kind hospitality during a three months research stay at the Division of Engineering and Applied Sciences, Harvard University.

*Also at Department of Physics, Harvard University, Cambridge, MA 02138.

[1] *Undercooled Metallic Melts, Properties, Solidification and Metastable Solid Phases*, edited by D. M. Herlach, I. Egry, P. Baeri, and F. Spaepen (Il Ciocco, Italy, 1993); Mater. Sci. Eng. A **178**, 1 (1994).
[2] W. Kurz and R. Trivedi, Acta Metall. Mater. **38**, 1 (1990).
[3] R. Willnecker, D. M. Herlach, and B. Feuerbacher, Phys. Rev. Lett. **62**, 2707 (1989).
[4] J. Lipton, W. Kurz, and R. Trivedi, Acta Metall. **35**, 957 (1987).
[5] W. J. Boettinger, S. R. Coriell, and R. Trivedi, in *Rapid Solidification Processing: Principles and Technologies IV*, edited by R. Mehrabian and P. A. Parrish (Claitor's, Baton Rouge, LA, 1988), p. 13.
[6] K. Eckler, R. F. Cochrane, D. M. Herlach, B. Feuerbacher, and M. Jurisch, Phys. Rev. B **45**, 5019 (1992).
[7] M. J. Aziz, J. Appl. Phys. **53**, 1158 (1982).
[8] M. J. Aziz and T. Kaplan, Acta Metall. **36**, 2335 (1988).
[9] M. J. Aziz, Metall. Mater. Trans. A **27**, 671 (1996).
[10] M. J. Aziz, J. Y. Tsao, M. O. Thompson, P. S. Peercy, and C. W. White, Phys. Rev. Lett. **56**, 2489 (1986).
[11] D. E. Hoglund, M. J. Aziz, S. R. Stiffler, M. O. Thompson, J. Y. Tsao, and P. S. Peercy, J. Cryst. Growth **109**, 107 (1991).
[12] P. M. Smith and M. J. Aziz, Acta Metall. Mater. **42**, 3515 (1994).
[13] M. J. Aziz and W. J. Boettinger, Acta Metall. Mater. **42**, 527 (1994).
[14] D. M. Herlach, Mater. Sci. Eng., R. **12**, 177 (1994).
[15] D. M. Herlach, R. Willnecker, and F. Gillessen, ESA Bull. **222**, 39 (1984).
[16] T. Volkmann, G. Wilde, R. Willnecker, and D. M. Herlach, J. Appl. Phys. **83**, 3028 (1998).
[17] E. Schleip, R. Willnecker, D. M. Herlach, and G. P. Gorler, Mater. Sci. Eng., A **98**, 39 (1988).
[18] D. Turnbull, Metall. Trans. A **12**, 695 (1981).
[19] S. R. Coriell and D. Turnbull, Acta Metall. **30**, 2135 (1982).
[20] F. Spaepen, Acta Metall. **23**, 729 (1975).
[21] F. Spaepen and R. B. Meyer, Scr. Metall. **10**, 37 (1976).
[22] J. S. Langer and H. Muller-Krumbhaar, Acta Metall. **26**, 1681 (1978).
[23] R. D. Doherty, B. Cantor, and S. J. M. Fairs, Metall. Trans. A **9**, 621 (1978).
[24] R. Trivedi and J. T. Mason, Metall. Trans. A **22**, 235 (1991).
[25] Y. Lee and A. Karma (unpublished).
[26] J. H. Bilgram, M. Firmann, and E. Hurlimann, J. Cryst. Growth **96**, 175 (1989).
[27] T. Iida and R. I. L. Guthrie, *The Physical Properties of Liquid Metals* (Oxford, Clarendon, 1988).
[28] T. B. Massalski, *Binary Alloy Phase Phase Diagrams* (American Society for Metals, Metals Park, OH, 1986), Vol. 2, p. 1779.
[29] G. J. Galvin, M. O. Thompson, J. W. Mayer, P. S. Peercy, R. B. Hammond, and N. Paulter, Phys. Rev. B **27**, 1079 (1983).
[30] J. Y. Tsao, S. T. Picraux, P. S. Peercy, and M. O. Thompson, Appl. Phys. Lett. **48**, 278 (1986).
[31] J. A. West, Ph.D. thesis, Harvard University, 1993.
[32] P.M. Smith, Ph.D. thesis, Harvard University, 1992.
[33] H. A. Atwater, J. A. West, P. M. Smith, M. J. Aziz, J. Y. Tsao, P. S. Peercy, and M. O. Thompson, in *Beam-Solid Interactions: Physical Phenomena*, edited by J. A. Knapp, P. Børgesen, and R. A. Zuhr, MRS Symposia Proceedings No. 157 (Materials Research Society, Pittsburgh, 1990), p. 369.
[34] D. E. Hoglund, M. O. Thompson, and M. J. Aziz, Phys. Rev. B **58**, 189 (1998).
[35] G. Lohöfer (unpublished).
[36] C. G. Levi and R. Mehrabian, Metall. Trans. B **11**, 21 (1980).
[37] S. Y. Shiraishi and R. G. Ward, Can. Metall. Q. **3**, 117 (1964).
[38] G. P. Görler and M. Schwarz (unpublished).